ADVANCED FUNCTIONAL MATERIALS
www.afm-journal.de

Real Time and Highly Sensitive Sub-Wavelength 2D Hybrid Perovskite Photodetectors

*Rosanna Mastria, Karl Jonas Riisnaes, Agnes Bacon, Ioannis Leontis, Hoi Tung Lam, Mohammed Ali Saleh Alshehri, David Colridge, Tsz Hin Edmund Chan, Adolfo De Sanctis, Luisa De Marco, Laura Polimeno, Annalisa Coriolano, Anna Moliterni, Vincent Olieric, Cinzia Giannini, Steven Hepplestone, Monica Felicia Craciun, and Saverio Russo**

Layered (2D) perovskites are an emerging attractive 2D system with enhanced stability to ambient conditions as opposed to their highly unstable three dimensional bulk counterpart. Their uniquely tuneable optical and electrical properties are underpinning a surge of interest in 2D-photovoltaics. So far, the development of nano-scale integrated opto-electronic 2D perovskite devices remains nearly unexplored since they have generally been found to be incompatible with standard top-down semiconductor nano-fabrication technologies. Here, following the synthesis of solvent-stable 2D-fluorinated phenethylammonium lead iodide perovskite $(F\text{-}PEA)_2PbI_4$ (F-PEAI), planar photodetectors entirely fabricated in atmosphere is demonstrated, exhibiting figures of merit rivalling those of commercial silicon photodiodes. A record large room temperature detectivity ($>5 \times 10^{17}$ Jones), a fast time photoresponse (rise time 1.5 ns), an extraordinarily large linear dynamic range (228 dB), as well as a photo-responsivity of $\approx 1100\ AW^{-1}$ are demonstrated for devices on a range of substrates including flexible wearable media without the need for any planarization or any atomically thin dielectric, in stark contrast to other 2D semiconductors. Finally, the suitability of nano-scale 2D F-PEAI photodetector arrays with sub-wavelength pixel size of just 100 nm of use for high definition imaging is demonstrated.

1. Introduction

The downscaling of photodetectors with high-end performance is needed for fast signal processing at the interface between photonic and electronic platforms. Such devices remain scarce owing to the lack of suitable materials able to fulfill the stringent photophysical and electronic requirements. Newly discovered perovskites may offer unprecedented opportunities owing to their strong light absorption[1] and long photo-excited carrier lifetimes[2] underpinning significant breakthroughs in photovoltaics,[3,4] transistor,[5] photo sensor,[6] light emitting diode,[7] and laser technologies.[8] Best known in their three dimensional bulk (3D) crystal form, perovskites have recently been synthesized in layered (2D) crystals consisting of alternating inorganic/organic layers. In these systems, charges are confined in the inorganic quantum wells underpinning a range of uniquely attractive properties.

R. Mastria, K. J. Riisnaes, A. Bacon, I. Leontis, H. T. Lam, M. A. S. Alshehri, D. Colridge, T. H. E. Chan, A. De Sanctis, S. Hepplestone, M. F. Craciun, S. Russo
Centre for Graphene Science
College of Engineering
Mathematics and Physical Sciences
University of Exeter
Exeter EX4 4QL, UK
E-mail: s.russo@exeter.ac.uk

L. De Marco, L. Polimeno, A. Coriolano
CNR NANOTEC - Institute of Nanotechnology
via Monteroni, Lecce 73100, Italy

A. Coriolano
Department of Mathematics and Physics 'E. De Giorgi'
University of Salento
via Monteroni, Lecce 73100, Italy

A. Moliterni, C. Giannini
CNR
Institute of Crystallography
Via Amendola, 122/O, Bari 70126, Italy

V. Olieric
Swiss Light Source
Paul Scherrer Institute
Villigen PSI 5232, Switzerland

The ORCID identification number(s) for the author(s) of this article can be found under https://doi.org/10.1002/adfm.202401903

DOI: 10.1002/adfm.202401903

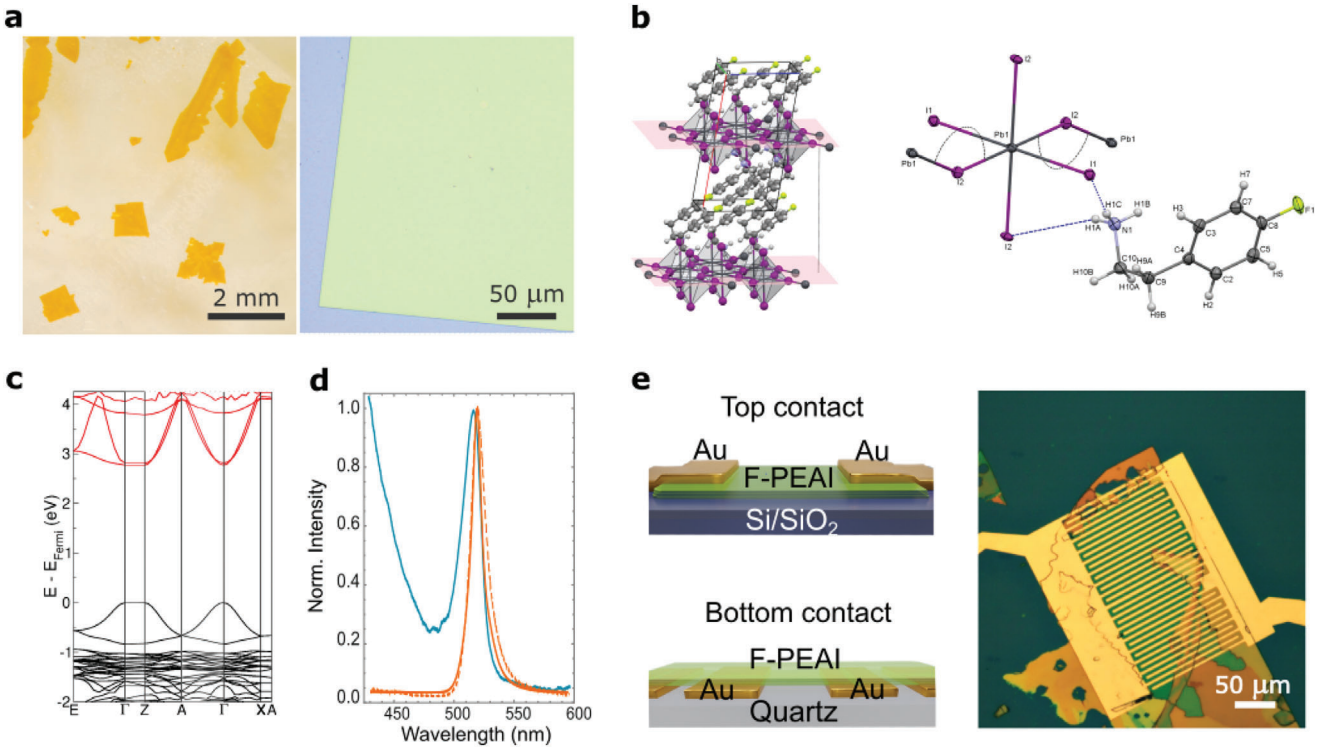

Figure 1. 2D F-PEAI crystal structure, optical characteristics, and photodetector fabrication. a) Photograph (left) and optical micrograph (right) of 2D F-PEAI single-crystallyne flakes. b) Crystal structure of 2D F-PEAI. Left: a view of the crystal packing and the two nearest least-squares planes (distanced by 16.30 Å) through the equatorial atoms of the PbI_6 octahedra. Right: A view of the asymmetric unit and its local environment showing four symmetry equivalent I atoms to complete the octahedron and two symmetry equivalent Pb atoms with the distortion of the in-plane inorganic layer, whilst the Pb–I–Pb angle is 151.928(8)°. The broken blue lines indicate two of the N—H···I hydrogen bonds. c) Calculated electronic band structure of pristine 2D F-PEAI. d) Plots of the measured absorption (dark cyan) and photoluminescence spectra (orange) of a representative mechanically exofliated 2D F-PEAI flake prior to (pristine, solid line) and after (dashed line) top-down lithographic fabrication of a photodetector device. e) Top and bottom contact device schematics and optical micrograph image of a top-down lithographically processed 2D F-PEAI photodetector.

These include high photoluminescence quantum yield,[6,9] tuneable optical, and electrical properties by composition,[10,11] narrow excitonic transitions with strong binding energies[12] ideally suited for room temperature non-linear operations in low input power polaritonic devices, and strong optical non linearities.[13] Presently, the full value of 2D hybrid perovskites in nano-scale optoelectronics is hardly explored due to their instability to ambient conditions and solvents commonly used in standard top-down semiconductor nano-fabrication technologies. This makes it arduous to develop perovskite-based competitive high-density and large bandwidth signal processing solutions.

Here, we demonstrate nano-scale 2D-fluorinated phenethylammonium lead iodide perovskite $(F\text{-}PEA)_2PbI_4$ (F-PEAI) planar photodetectors entirely fabricated in atmosphere and using standard electron beam lithography involving the use of solvents. The devices reproducibly display outstanding figures of merit reaching a room temperature detectivity $>5 \times 10^{17}$ Jones, a real-time photoresponse comparable to that of commercial 2 GHz Si photodiode, an extraordinarily large linear dynamic range (228 dB), as well as a photo-responsivity of $\approx$1100 AW^{-1}. These photodetectors are stable from room-temperature down to 4 K and they can be reliably fabricated on a wide range of substrates including flexible wearable media with no loss of performance and without the need for any planarization steps nor the need to use atomically clean dielectrics, in stark contrast to other 2D materials such as graphene and transition metal dichalcogenides. Finally, we demonstrate working planar nano-scale 2D F-PEAI photodetectors of sub-wavelength size smaller than a fifth of the wavelength of the detected light, thereby paving the way to the use of perovskites for high definition imaging technologies.

2. Results and Discussion

Layered perovskite crystals consist of alternating sheets of inorganic $[PbX_4]^{2-}$ anions (with the halogen X = Cl, Br, or I) and organic alkylammonium cations (**Figure 1**a,b) which can be synthesised by low-cost and scalable wet chemistry processes.[14] The inorganic layer dominates the physics of the lowest-energy electronic excitations, while the organic part behaves as a potential barrier resulting in the confinement of charges in the plane of the inorganic layer, i.e., quantum well.[11,15,16] In these crystals, both the energy bandgap and the exciton binding energies are a function of the thickness of the quantum well, which depends on the number "n" of inorganic layers, going from a 2D system with a single inorganic layer sandwiched between two organic spacers (n = 1) to a quasi-2D system with higher "n" number (n $\geqslant$ 2).[14] Previous studies have highlighted that the polar nature of perovskites results in the quick decomposition of the

anionic metal-halide and cationic organic upon exposure to ambient moisture or a solution consisting of polar solvents, making it difficult to fabricate high quality devices in ambient conditions using standard semiconductor nano-scale processing.[17–19] In 2D perovskites, the presence of bulky hydrophobic cations, instead of the small organic cations like in 3D perovskites, provides enhanced resistance to ambient condition.[20] In addition, the crystal structure of 2D perovskites can be effectively engineered through careful selection of organic cations, leading to a significant improvement in their structural stability. For instance, the use of benzene-based cations leads to more organized and stable structures than those obtained with aliphatic species, as well as, by modifying the organic spacer molecule either by hydrogen bonding between organic layers or fluorination of the common spacer molecule $C_6H_5C_2H_4NH_3$ (phenethylammonium, PEA) results in improved stability of these materials.[21–24] Furthermore, fluorination strongly influences the arrangement of the aromatic ring of PEA molecules in the 2D hybrid perovskite crystal resulting in a better alignment of the inorganic layers thereby enhancing the out of plane charge transport.[25] To date, most of the demonstrated perovskite-based devices have been fabricated using quasi-2D or 3D-single crystals using solvent-free methods such as shadow mask deposition or lamination on prepatterned electrodes in which slow time responses (from 0.1 µs to 0.5 ms[26,27]) have been reported for photodetector surface areas of several square millimeters, i.e., one million times larger than the state-of-the-art pixels found in commercial CCDs, making them unsuitable for high resolution imaging.

In this study thin 2D perovskite flakes of F-PEAI were grown by the antisolvent vapor-assisted crystallization method at room temperature[28] and subsequently exfoliated in ambient conditions onto various substrates such as Si coated by 200 nm thick SiO_2, quartz and flexible PET, see Figure 1a. Single-crystal X-ray diffraction has been performed on the as-synthesized flakes at a synchrotron facility (see Section S1, Supporting Information). Figure 1b shows a view of the asymmetric unit and its local environment with the octahedral coordination of the Pb atom and the in-plane distortion of the inorganic chain. The crystal packing is characterized by alternating corner-sharing $[PbI_6]^{2-}$ octahedra layers and double layers of fluorophenethylammonium cations with the orientation along the longest stacking axis (i.e., the a axis) corresponding to that of the inorganic layers (see Figure 1b; Section S1, Supporting Information). The interplanar distance between two nearest least-squares planes through the equatorial atoms of the PbI_6 octahedra was 16.30 Å, similarly to previously reported values.[29,30] The presence of directional hydrogen bonds influences the crystal packing resulting in the inorganic chain distortion:[14,29] the PbI_6 octahedra were in-plane distorted and, similarly to literature results,[29] the in–plane Pb–I–Pb angle was 151.928(8)° (see Figure 1b) and responsible for an in-plane rotation of the inorganic octahedra.[31] The range for the Pb–I octahedral bonds lengths and the I_{ap}–Pb–I_{eq} octahedral bond angles was 3.1486(4) - 3.2170(5) Å and 86.954(12) –93.046(12)°, respectively, with I_{ap} and I_{eq} the equatorial and apex I atoms of the octahedron, respectively (see Section S1, Supporting Information). The band structure of this material calculated from first principles using density functional theory, as implemented in VASP,[32] with the HSE06 functional[33] (see Sections S2 and S3, Supporting Information) is shown in Figure 1c. Optical absorption spectroscopy measurements reveal that the large energy gap makes this 2D perovskite an excellent absorber of ultraviolet wavelength light whilst strongly-bound excitons in ambient conditions dominate the optical absorption below the single particle bandgap giving rise to a photoluminescence (PL) peak at 523 nm,[22] see Figure 1d and Section S4 (Supporting Information). This strong PL feature provides a quick and reliable insight on the 2D crystals such as their resilience to solvents and other device fabrication conditions. Indeed, the physics of 2D excitons underpinning the PL peak is highly sensitive to changes in the 1) crystal structure (e.g., strain[34] and defects[35]), 2) dielectric properties,[36] and 3) quantum well structure.[21] To this end, we have explored a wide range of solvents (i.e., xylene, hexane, toluene, chlorobenzene, water, isopropryl alcohol, and anisole) and fabrication conditions, and we have identified the best combination of chemicals and processing parameters (see Experimental Section), which result in fully processed nano-scale devices with nearly unchanged PL peak energy and full width at half maximum (FWHM), see Figure 1d and Section S4 (Supporting Information). Hence, we employed these chemicals and solvents for the deterministic top-down (top-contacts) fabrication of micro- and nano-meter scale metal structures onto a ≈150 nm thick 2D F-PEAI flake by standard electron-beam lithography, metal deposition, and lift-off in ambient conditions, see Figure 1e and Section S4 (Supporting Information). In addition, we fabricated control devices by lithography-free lamination of 2D F-PEAI crystals onto prepatterned contacts (bottom-contacts) following established techniques for the dry transfer of other 2D materials, see Figure 1e.

Figure 2a,b shows the room temperature source-drain bias-dependent (V_{sd}) current measured in the dark and under illumination with three distinct laser wavelengths (λ = 375, 473, and 514 nm in red, blue, and green, respectively) for two representative top- and bottom-contacts devices, respectively. Both device types show a large bias-dependent photoresponse upon illuminating with the 375 and 514 nm lasers. Similar levels of photocurrent are observed for devices which employ different metal contacts such as the high melting point and low diffusivity MoRe alloy (see Section S5, Supporting Information) and in a total of more than 15 devices (see Section S6, Supporting Information) fabricated using F-PEAI crystals from five different growths. These experimental observations suggest a strong role of the F-PEAI energy levels on the measured photocurrent, with photo-excitation of free charge carriers upon absorption of photons with energy larger than the single particle energy gap. By contrast, one would expect to measure no photocurrent when illuminating with the 514 nm laser, since the absorption of these photons generates strongly-bound charge neutral excitons (see Figure 1c,d), which should not respond to an in-plane electric field and whose large binding energy (≈540 meV, see Experimental Section) prevents their splitting into free carriers at room temperature, and yet a bias-dependent photocurrent is measured.[37]

Several potential mechanisms exist which could enable the splitting of the excitons. For example contact-induced defect states, e.g., Au substitution of Pb atoms in the F-PEAI, could provide a ladder of energy states supporting the efficient exciton splitting into free carriers through the reduction of their binding energy, see Sections S2 and S3 (Supporting Information). However, the fact that we observe a similar photoresponse in

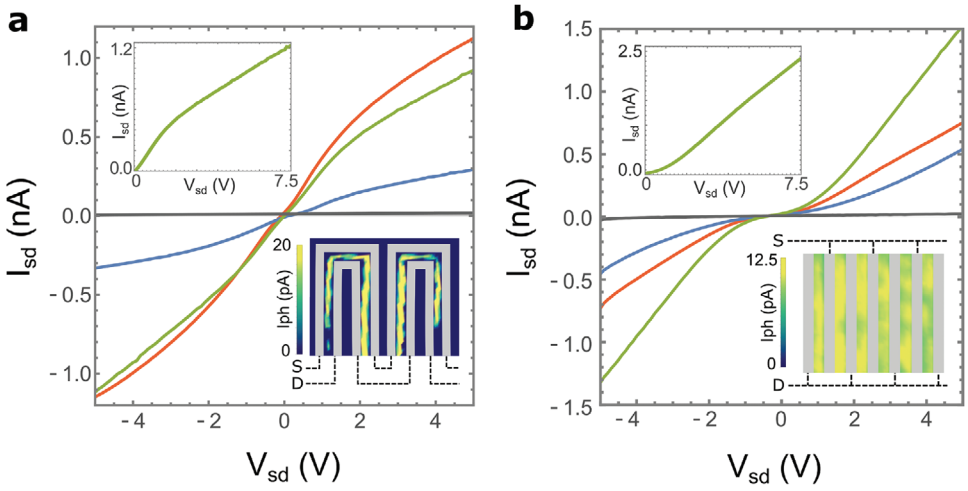

Figure 2. Photocurrent characteristics and maps of photo-active areas. Panels (a,b): Plots of current versus voltage characteristics for bottom (a) and top-contact (b) 2D F-PEAI photodetectors measured in the dark (black) and under continuous wave laser illumination λ = 375, 473, and 514 nm represented in red, blue and green, respectively (a) laser diameter $d_\lambda \approx 30$ µm and irradiance $I = 134$ µW cm^{-2}; b) $d_\lambda \approx 190$ µm and $I = 91$ µW cm^{-2}). The photoresponsive areas are $A_{ph} = 8 \times 10^{-8}$ cm^2 (a) and 8.5×10^{-5} cm^2 (b). Top insets: Current versus voltage characteristics up to V_{SD} = 7.5 V under 514 nm laser illumination. Bottom insets: Colorplots of spatially resolved photocurrent acquired for a fixed V_{SD} = 5 V and by rastering a focussed laser ($I = 46$ W cm^{-2}, $\lambda = 514$ nm, $d_\lambda \approx 0.5$ µm corresponding to a photoresponsive area $A_{ph} = \pi(d_\lambda/2)^2$). The gray lines correspond to the source and drain electrodes. The width of the electrodes and the channel length are 3 µm.

devices fabricated with different metals (Au and MoRe) and in photodetectors fabricated with very different methods, i.e., top-down lithography and non-invasive bottom-contacts, suggest that a different exciton splitting mechanism, which does not involve interdiffusion of the metal contacts may be dominating the photoresponse in these 2D crystals. Recent studies on excitons in other 2D semiconductors have demonstrated that the binding energy of these quasiparticles is highly sensitive to the dielectric environment,[36] and this could drive a full quenching of the exciton binding energy in the vicinity of the metal contacts enabling the splitting of charge neutral excitons into free carriers. However, such a mechanism cannot explain the large photocurrent measured when illuminating the middle of the F-PEAI channel, away from the contacts (see Figure 2a,b and Section S7, Supporting Information). This experimental observation suggests that defects present in the bulk of the crystal, such as those introduced during the synthesis, are responsible for the efficient splitting of excitons. Following this hypothesis, several defects were considered via DFT (see Sections S2 and S3, Supporting Information) and the iodine vacancy was identified as most likely. The predicted defect states are close to the band edge, contributing to a broadening of the optical absorption edge consistently with the experimental observations. Recent studies have showed that the formation of polarons constitute an alternative intrinsic mechanism leading to the efficient splitting of excitons.[38] However, in the absence of defects the polaron-assisted splitting is not expected to lead to any internal gain mechanism in photodetectors. Hence, a study of the figures of merit of these devices can shed light on the role of the exciton splitting mechanism.

Figure 3a shows that the photoresponsivity of the 2D F-PEAI planar photodetectors reaches 1120 AW^{-1} at 2×10^{-12} W cm^{-2} for the bottom-contact and >240 AW^{-1} for the top-contact configuration, with the slightly differing performance due to a different metal/2D F-PEAI contact interface. Such large values are one order of magnitude higher than the values reported in 2D perovskites to date and ≈ 5000 times larger than ever reported for a planar perovskite device fabricated by using electron beam lithography.[18] Upon increasing the irradiance the photoresponsivity decreases monotonously due to the filling of deep defect states[39] and exciton–exciton annihilation[40] as previously reported.[41] Interestingly, the external quantum efficiency of 2D F-PEAI greatly exceeds one for both structures and it increases monotonously upon reducing the irradiance (see Figure 3b), indicating the presence of an internal gain mechanism.

Earlier studies on 2D hybrid graphene photodetectors have shown that charge recirculation and trapping can lead to very large gain (>10^8),[42] and shallow traps have been shown to support >6 orders magnitude faster time response than that of deep traps, whilst still retaining a small gain.[43] Therefore, in 2D F-PEAI shallow trap states may play the dual role of 1) splitting the strongly bound electron-hole pairs and 2) enabling internal gain for irradiance <2×10^{-8} W cm^{-2}. In addition, previous studies on metal/semiconductor/metal structures have shown that the injection/extraction of charge across the semiconductor/metal contacts is affected by the modification of the Schottky barrier due to the optically generated carriers.[44] In this case a strongly unbalanced electron/hole carriers transport leads to an accumulation of holes at the anode. As a result, the image force of the accumulated holes at the contact lowers the height of Schottky barrier boosting the external quantum efficiency to >100%. This is a likely scenario for 2D F-PEAI due to the presence of shallow traps affecting one carrier type.

To quantify the sensitivity of these photodetectors, we characterize their photodetectivity and noise spectral density, see Figure 3c. We find that both device types exhibit very low values of intrinsic electric noise, which results in room temperature values of photodetectivity as large as 5.5×10^{17} Jones at a few picowatts of irradiance and considering a spectral noise density of

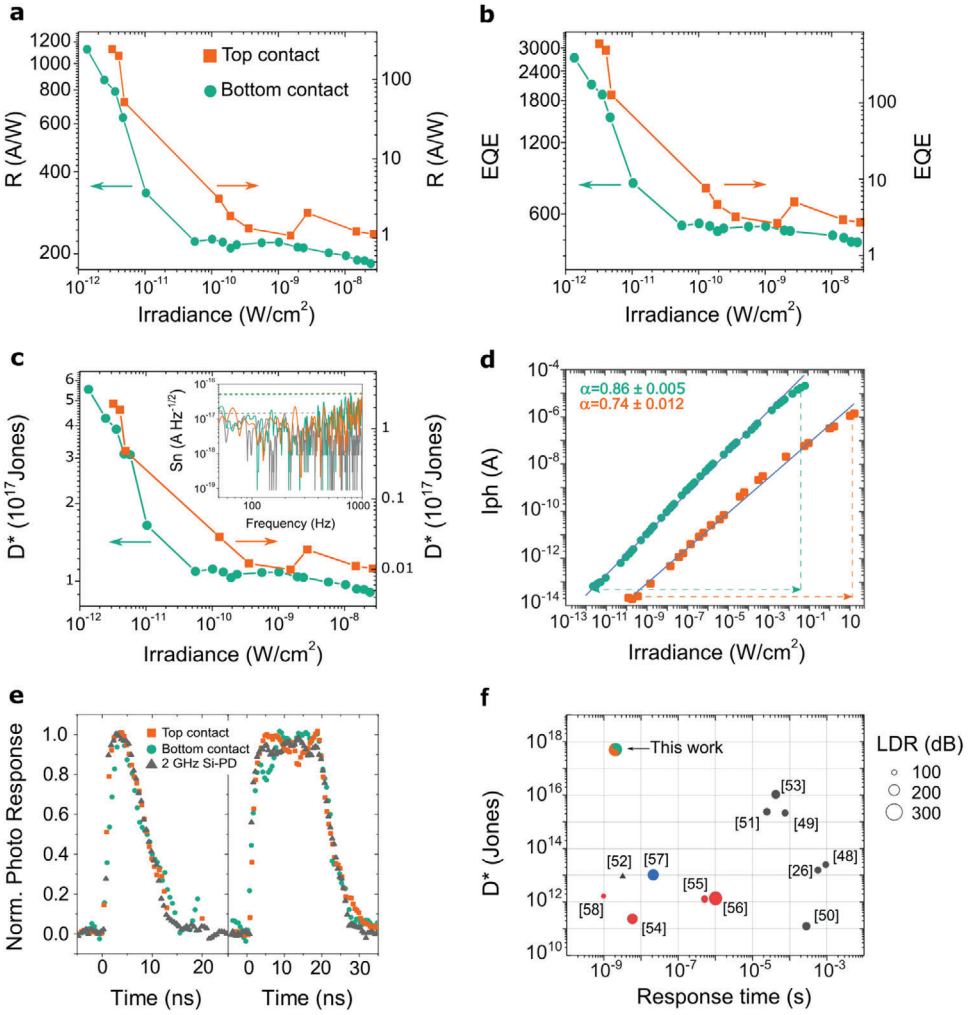

Figure 3. Figures of merit of 2D F-PEAI photodetectors. a) Plot of the power dependent photoresponsivity of top-contact (orange squares) and bottom-contact (green circles) 2D F-PEAI photodetectors measured at V_{sd} = 7.5 V (orange) and 5 V (green) at room temperature, under uniform illumination (λ = 514 nm, $d_\lambda \approx$ 650 µm and $A_{ph} = 4.9 \times 10^{-5}$ cm^2 and 8.5×10^{-5} cm^2 for bottom and top-contact device, respectively). b) External quantum efficiency for the photodetectors in (a). c) Plot of the photodetectivity for the devices in (a) and their noise spectral density (inset). Dashed green and yellow lines indicate the highest level of the measured noise spectral density which is then used to estimate the detectivity. d) Plot of the linear dynamic range (LDR) measured in the same devices of (a) at V_{sd} = 5 V under continuous laser illumination (λ = 514 nm). e) Representative measurements of the time response for the devices in (a) (green and orange) at V_{sd} = 20 V and for a commercial 2 GHz silicon photodiode (Si-PD) (gray) (λ = 405 nm, laser pulses of 6 and 21 ns), see Experimental Section for more details. f) Plot of detectivity versus response time of state-of-the-art perovskite based photodetectors compared to this work. Gray, red and blue circles represents 2D single crystal, thin-film, and all-inorganic perovskite based devices, respectively. Triangles represent studies where LDR were not quoted.

4.5×10^{-17} AHz$^{-1/2}$ (see Section S6, Supporting Information). Such large values of detectivity rivals that of makes these planar 2D photodetectors very attractive for applications in extremely low-light conditions. At the same time, we observe a linear scaling of the photocurrent as a function of the irradiance (Iph $\propto$ P$^\alpha$) over a range of 11 decades corresponding to 228 dB, that is from ultra-dim illumination more than 1000 times dimmer than a typical moonless starlit sky to an ultra-bright source equivalent to a staggering 100 suns.[45] Based on prior studies,[46] systems with trap-induced unbalanced transport are expected to display a LDR with $\alpha \approx 0.75$ towards high irradiance. This is likely to be the case for photodetectors with top- rather than bottom-contacts since the metal deposition on organic semiconductors is well-known to introduce defect states at the metal/organic interface. Finally, we characterize the time response of these devices by measuring the photocurrent generated upon illumination with ultra-fast laser pulses, and benchmark the F-PEAI performance against that of a commercial 2 GHz bandwidth Si photodiode, see Figure 3e. In this experiment we employ a sufficiently high laser irradiance (100 W cm^{-2}) to eliminate the need of any external current amplifier, which would affect the measurements, see Experimental Section. At the same time, at high irradiance charge traps are saturated by photo-excited carriers supporting a fast time response albeit without an internal gain. Both the 2D F-PEAI device types have a similar rise time to that of the 2GHz Si photodiode. In these devices, charges achieve a drift velocity of ≈3000 ms^{-1} under the action of an electric field of ≈6 MVm^{-1} (channel length 3 µm at a bias of 20 V). A measured transit time of ≈ 1 ns

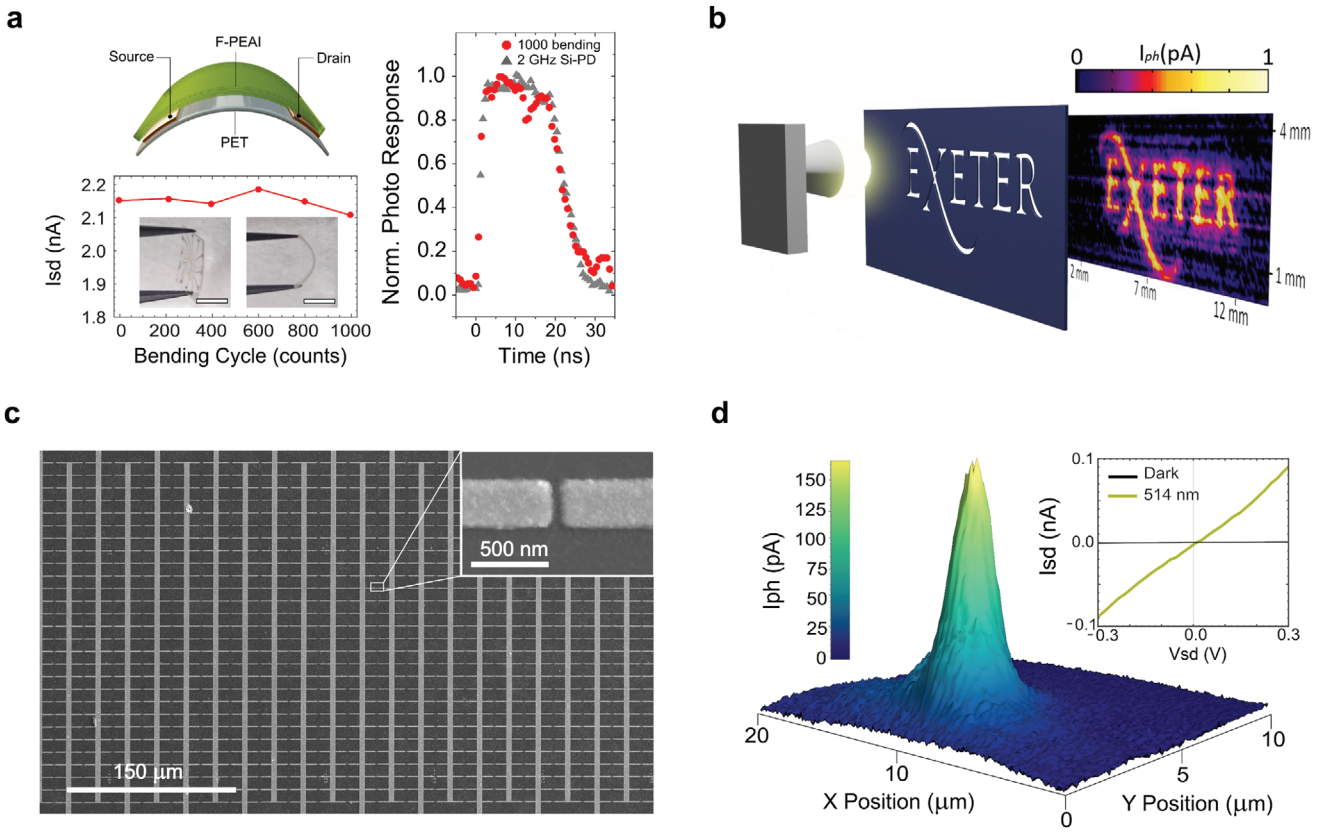

Figure 4. a) Top left: schematic of 2D F-PEAI photodetector on flexible PET. Bottom left: plot of the photocurrent measured after subsequent bending cycles for the device shown in the pictures (white scale bars are 5 mm, $\lambda = 514$ nm, $d_\lambda \approx 30$ µm, $I = 120$ µWcm^{-2}, $A_{ph} = 6 \times 10^{-7}$ cm^2, $V_{sd} = 5$ V). Right: time response after 1000 bending cycles (red) for a laser pulse ($\lambda = 405$ nm) with duration of 37ns and fixed bias $V_{sd} = 20$ V, and for a commercial 2 GHz silicon photodiode (gray). Bending cycles were performed in atmosphere conditions. Bending radius ≈ 3.5 mm, bending angle 150°, see methods. b) Image of the logo of the University of Exeter acquired using a 2D F-PEAI photodetector (pixel area 137 µm^2 and bias $V_{sd} = 3$ V). c) Scanning electron microscope image of a 11 × 28 array of photodetector pixels with 100 nm channel length as shown in the inset. d) Image of the 514 nm laser beam shape acquired by rastering a single sub-wavelength 100 nm photodetector pixel in 100 nm steps. Inset: Plot of the current versus voltage of the 100 nm photodetector pixel ($\lambda = 514$ nm, $I = 46$ W cm^{-2}, $d_\lambda \approx 0.5$ µm).

suggests that the charge carrier mobility is higher than 5 cm^2 Vs^{-1}, which is consistent with high quality single crystal structure reported by other authors.[47]

A comparison of the main figures of merit for our devices against the comparative group of 2D and 3D perovskite devices exhibiting nano-second rise time reveals that F-PEAI photodetectors exhibit more than 10000 times larger detectivity and two times larger LDR than current state-of-the-art devices.[26,48–61] Crucially, 2D F-PEAI photodetectors are 10^8 times faster than their unfluorinated counterpart fabricated by using lithography,[18] and they also have a four decades larger LDR than previously reported in 2D perovskite photodetectors.[50] Such extraordinary device performance makes 2D F-PEAI planar structures comparable or superior to research grade commercial Si or InGaAs photodetectors.[62] These devices are also stable to thermal cycling over a wide temperature range from room temperature down to 4 K, see Section S4 (Supporting Information). To explore the extent of possible uses of 2D F-PEAI photodetectors behind the confines of rigid substrates, we have fabricated devices on mechanically flexible PET commonly used for wearable technologies, see **Figure** 4a. Surprisingly, we find that even after subduing the devices to ≈ 1000 bending cycles in atmosphere conditions, they retain the outstanding performances including the ultra-fast time response, which seamlessly follows the rise and fall-time of the ultra-fast laser pulse measured using a commercial 2 GHz bandwidth Si photodiode, see Figure 4a. Furthermore, Figure 4b shows that these photodetectors can easily be used for imaging technologies. Here, a F-PEAI photodetector is rastered underneath a back-lit University of Exeter logo producing the electronic image representation as seen on the right side of the figure (Figure 4b), see Experimental Section. Finally, to test the suitability of 2D F-PEAI to nano-scale integration of opto-electronic components, we have fabricated arrays of planar photodetectors (see Figure 4c) with sub-wavelength photo-active channels as small as 100 nm, that is more than ten times smaller than the typical size of nowadays flagship commercial CCD and CMOS camera pixels (>1 µm), see Experimental Section and Section S8 (Supporting Information). Figure 4d shows that these nano-pixels addressed individually with a focused laser beam display a proportionally large photocurrent even when illuminated with photons of wavelengths five times larger than their geometrical size. Hence, we utilize such a nano-pixel to image a laser

beam profile (λ = 514 nm) with a spatial resolution of 100 nm, demonstrating the use of 2D F-PEAI in high-definition imaging.

3. Conclusion

In conclusion, we have demonstrated nano-scale 2D-fluorinated phenethylammonium lead iodide perovskite planar photodetectors entirely fabricated in atmosphere and using standard electron beam lithography involving the use of solvents. These devices display a staggering range of parameters rivaling the figures of merit of other commercially established leading technologies. A record large room temperature detectivity (>5 × 10^{17} Jones) and a fast photoresponse are accompanied by an extraordinarily large linear dynamic range (228 dB) and a photoresponsivity of ≈1100 AW^{-1}. Crucially these photodetectors are compatible with a wide range of substrates including flexible wearable media with no loss of performance. Finally, we show that arrays of 2D F-PEAI sub-wavelength nano-pixels of sub-visible wavelength size of just 100 nm can be reliably used for high definition imaging.)

4. Experimental Section

Lithography: The optimized nano-scale processing consists of coating the substrates with a ≈400 nm thick layer of Poly(methyl methacrylate) (PMMA) (495K A6 in anisole) followed by baking on a hot plate for 20 min at 60°C. The electron-beam exposed PMMA was developed in a solution of hexane:toluene = 30:13 for 10 s followed by electron beam evaporation of Ti/Au (5/50 nm), lift-off in chlorobenzene for 5 min and rinsing in hexane all at room temperature.

For the pre-patterned contacts, substrates were coated with ≈600nm of 495K A6 PMMA and baked for 1 min at 180°C. After e-beam exposure, these samples were developed using a solution of IPA:MIBK:MEK in a ratio of 15:5:1 for 30 s, and then rinsed in IPA. Metals are then deposited via e-beam evaporation of Ti/Au (5/30 nm), followed by lift-off in warm acetone (at 70°C) for 1 h.

4.0.0.1. $(F\text{-}PEA)_2PbI_4$ Single Crystals: F-PEAI single crystals were synthesized with antisolvent vapor-assisted crystallization, a simple, one-step method carried out at room temperature. 230.5 mg PbI_2 and 267 mg 4-Fluoro-Phenethylammonium iodide were dissolved in 1 mL GBL and stirred at 70 °C for 30 min. Precursors solutions were prepared in an N_2-filled glovebox. 2D perovskite single crystals were synthesized as follows: glass slides were cleaned with acetone and water in ultrasonic bath for 10 min each and then soaked into a TL1 washing solution ($H_2O_2/NH_3/H_2O$ 1:1:5, v/v), heated at 80 °C for 10 min to remove organic contamination and finally rinsed ten times in water. The perovskite solution (2 µL) was deposited on the top of the substrate and immediately covered by the second glass substrate. Then, a small vial containing 2 mL of dichloromethane (DCM) was placed on top of the two sandwiched substrates. The two sandwiched substrates and the vial containing DCM were placed in a bigger Teflon vial, closed with a screw cap and left undisturbed. After 12 h millimeter-sized crystals appeared in between the two substrates having a thickness varying from a few to ten micrometres. Atomic force microscopy measurements on the 2D $(F\text{-}PEAI)_2PbI_4$ were carried out with a commercial AFM system (Bruker Dimension Icon XR) using a SiN cantilever (PFQNE-AL) with a resonance frequency of 300 kHz and a Si tip (curvature of 5 – 12 nm), see Section S9 (Supporting Information).

Synchrotron Single Crystal X-Ray Diffraction: The single-crystal X-ray diffraction data measurements for F-PEAI were carried out at the beamline PXIII (X06DA-PXIII, http://www.psi.ch/sls/pxiii/) at the Swiss Light Source (SLS), Villigen, Switzerland, using a Parallel Robotics Inspired (PRIGo) multiaxis goniometer[63] and a Pilatus 2M-F detector. Data collection was performed at low temperature (T=100 K) with a 90 × 50 µm^2 beam at an energy of 17 keV (λ = 0.729317 Å) on a selected crystal mounted on litholoops (Molecular Dimensions). A 360° data set was collected in shutterless mode in steps of 0.5° at a speed of 0.25 s/step. Diffraction data were processed and corrected for absorption using XDS,[64] a data reduction software based on eight subroutines; the integrated intensities were scaled and corrected for absorption effects by the XSCALE subroutine.[64] Data collection, processing and main structure refinement details are provided in Table S1 (Supporting Information) of Section S1 (Supporting Information).

Technical Aspects of the Device Characterization: The room temperature spectroscopic, photocurrent and real-time measurements were acquired using a custom-built optoelectronic characterization system optimized to probe the photophysical properties of 2D materials.[65] The system embeds a number of solid state laser sources (Coherent OBIS 375LX, 473LS, 514LX, and 561LS and Omicron LuxX 685, with powers ranging from 30 to 50 mW). Each laser was digitally modulated and the power was adjusted using an analog signal. Custom-built drop-in-filter systems were used to introduce commercial neutral density, polarisers, notch, and bandpass filters in the optical path of the lasers and the microscope. The spectrometer was a Princeton Instruments Acton SP2500, equipped with three dispersion gratings (1200 gmm^{-1} with 500 nm and 750 nm blaze, and 1800 gmm^{-1} with 500 nm blaze) and it was equipped with a Princeton Instruments PIXIS400-eXcelon back-illuminated, Peltier cooled, CCD camera. The optical path could be configured for Raman, photoluminesce, and transmission/reflection spectroscopy and laser light illumination for photocurrent maps simply by replacing or removing the appropriate filters. The sample stage is a Prior Scientific OptiScan ES111 with a ProScan III controller with a minimum step size of 100 nm, enabling the accurate control of focused laser light for photocurrent maps with a spatial resolution of 1.2 × 10^{-9} cm^2 limited by the laser beam diameter. Calibrated power meters and fast photodetectors were used to measure the light intensity. For the time resolved photocurrent measurements a pulsed laser source (λ = 405 nm, Thorlabs NPL41B - Nanosecond Pulsed Laser Diode System). The transient voltage was measured using a real-time digital oscilloscope (Rohde & Schwarz 2 GHz Series 1000 Digital Oscilloscope). The use of such a fast oscilloscope, makes it possible to eliminate any amplifier from the measurement circuit, which was ideal as amplifiers tend to introduce spurious limitations to the bandwidth. On the other hand, the limited voltage resolution of the oscilloscope (≈1 mV) normally requires the use of high irradiance in photodetectors and large bias. For these reasons the fast time reponse was measured utilizing the NPL41B-Nanosecond Pulsed Laser at high irradiance of 100 Wcm−2 whilst applying a source-drain bias of 20 V across the device. The commercial photodiode used to benchmark the F-PEAI photodetectors was a Thorlabs DET025A/M (Si) with a rise/fall time of 0.150ns.The device performance did not change after the measurements with the pulsed laser. The cryogenic opto-electronic characterization was carried out in a liquid He ICE Oxford cryogenic set up with a cryo-compatible incoherent UV light source (400nm). Each photodetector had been exposed for a minimum of 400 h of continuous illumination and they have been subjected to several thermal cycles from room temperature down to 4.2K showing ⩽5% change of the measured relative photocurrent after the third thermal cycle, see Section S4 (Supporting Information). The electronic image of the Exeter University logo was obtained by mounting a 2D F-PEAI pixel on a microscope stage and rastering it underneath a back-lit mask with a negative of the logo of the University of Exeter and using an incoherent LED white light source. Finally, the bending tests where conducted in ambient conditions, and by pressing the substrates against a rod of radius ≈ 3.5 mm achieving a bending angle 150°.

Density Functional Theory Calculations: The first principles investigation was performed using the VASP density functional theory package. This approach was based upon a plane-wave basis set with project augmented wave (PAW) pseudopotentials. The Generalized Gradient Approximation (GGA) was used for the exchange-correlation potential with a PBE framework.[66] In order to more accurately estimate the electronic structure, the hybrid functional HSE06[33] was applied after the GGA relaxation. Since organic molecules are present, D3 correction was also applied to account for the van der Waal interactions. Valence electrons were modeled for the elements as followed, $2s^22p^2$ in C, $1s^1$ in H, $5s^25p^5$ in I, $4s^24p^5$

in Br, $2s^2 2p^3$ in N, $6s^2 6p^2$ in Pb and $6s^2 5d^9$ in Au, respectively. All calculations use an energy cut-off of 700 eV. In the relaxation calculations, the structures were considered relaxed when the maximum force acting on any atom was within 5 meVÅ^{-1} and a $3 \times 3 \times 1$ ($12 \times 12 \times 4$) Monkhorst Pack grid of k-points for relaxations (calculation of electronic properties) was used. To calculate the absorption spectra,the approach of Tsai was followed,[67] which did not include many body effects necessary to capture excitonic behavior.

Exciton Binding Energy: Assuming a conduction band edge at 425 ± 10 nm[68] corresponding to the DFT calculations $E_{cbe} \approx 2.90 \pm 0.05$ eV, and the exciton line at 523 ± 10 nm $E_{ex} = 2.37$ eV, the binding energy of the exciton can be estimated $E_b = E_{cbe} - E_{ex} = 540 \pm 10$ meV consistent with previously reported values.[69] The calculations show the exciton reduced mass is 0.177 (0.135 using PBE functional).

Supporting Information

Supporting Information is available from the Wiley Online Library or from the author.

Acknowledgements

R.M. acknowledged financial support from the European Commission Marie Curie Individual Fellowships (grant no. 843136). K.J.R. acknowledged financial support from EPSRC Center for doctoral training in Metamaterials (Grant no. EP/L015331/1) and the 1966 Scholarship. S.R. and M.F.C. acknowledge financial support from EPSRC (Grant no. EP/K010050/1, EP/M001024/1, EP/M002438/1, and EP/Y021339/1), from The Leverhulme trust (grants "Graded excitonics" and "Giant Permittivity"), and from "TERASSE" EU-H2020-MSCA-RISE (Grant no. 823878). S.P.H. and E. C. acknowledged via the membership of the UK's HEC Materials Chemistry Consortium, which is funded by EPSRC (EP/L000202, EP/R029431), this work used the ARCHER 167 UK National Supercomputing Service (http://www.archer.ac.uk). L.D.M., A.C., and L.P. gratefully acknowledged the project "Progetto Tecnopolo per la Medicina di precisione", grant number: Deliberazione della Giunta Regionale n. 2117 del 21/11/2018 founded by Apulia Region. [Correction added on May 15, 2024, after first online publication: The equal contribution of the authors has been updated in this version.]

Conflict of Interest

The authors declare no conflict of interest.

Author Contributions

R.M. and K.J.R. contributed equally to this work. RM and KJR conducting the fabrication, characterization, and data analysis of laminated and lithographically defined devices, respectively. IL characterized the photodetectors at cryogenic temperatures. AB fabricated devices on quartz and flexible substrates, as well as 3D printed parts. HTL conducted SEM and AFM characterization. DC, ADS, and AB contributed to develop the photocurrent characterization tool. LDM, LP, and AC have grown 2D perovskites. AM and CG performed the structure characterization by synchrotron single-crystal X-ray diffraction data. VO carried out the synchrotron single-crystal X-ray diffraction measurements. THEC and SH have conducted the DFT simulations. MFC and SR planned and directed the experiments and the interpretation of their results. All authors contributed to the writing of the article.

Data Availability Statement

The data that support the findings of this study are available from the corresponding author upon reasonable request.

Keywords

2D materials, organic electronics, perovskites, photodetectors

Received: January 31, 2024
Revised: March 22, 2024
Published online: May 6, 2024

[1] J. K. Zaręba, M. Nyk, M. Samoć, *Adv. Opt. Mater.* **2021**, *9*, 2100216.
[2] J. Guo, B. Wang, D. Lu, T. Wang, T. Liu, R. Wang, X. Dong, T. Zhou, N. Zheng, Q. Fu, Z. Xie, X. Wan, G. Xing, Y. Chen, Y. Liu, *Adv. Mater.* **2023**, *35*, 2212126.
[3] N. G. Park, *J. Phys. Chem. Lett.* **2013**, *4*, 2423.
[4] Best Research-Cell Efficiency Chart, photovoltaic research, nrel, https://www.nrel.gov/pv/cell-efficiency.html, (accessed: March 2024).
[5] A. Liu, H. Zhu, S. Bai, Y. Reo, M. Caironi, A. Petrozza, L. Dou, Y.-Y. Noh, *Nat. Electron.* **2023**, *6*, 559.
[6] K. Wang, J. Y. Park, Akriti, L. Dou, *EcoMat* **2021**, *3*, e12104.
[7] A. Fakharuddin, M. K. Gangishetty, M. Abdi-Jalebi, S.-H. Chin, A. R. bin Mohd Yusoff, D. N. Congreve, W. Tress, F. Deschler, M. Vasilopoulou, H. J. Bolink, *Nat. Electron.* **2022**, *5*, 203.
[8] J. Moon, Y. Mehta, K. Gundogdu, F. So, Q. Gu, *Adv. Mater.* **2023**, *n/a*, 2211284.
[9] X. Gong, O. Voznyy, A. Jain, W. Liu, R. Sabatini, Z. Piontkowski, G. Walters, G. Bappi, S. Nokhrin, O. Bushuyev, M. Yuan, R. Comin, D. McCamant, S. O. Kelley, E. H. Sargent, *Nat. Mater.* **2018**, *17*, 550.
[10] M. P. Arciniegas, L. Manna, *ACS Energy Lett.* **2022**, *7*, 2944.
[11] A. O. El-Ballouli, O. M. Bakr, O. F. Mohammed, *J. Phys. Chem. Lett.* **2020**, *11*, 5705.
[12] J.-C. Blancon, A. V. Stier, H. Tsai, W. Nie, C. C. Stoumpos, B. Traoré, L. Pedesseau, M. Kepenekian, F. Katsutani, G. T. Noe, J. Kono, S. Tretiak, S. A. Crooker, C. Katan, M. G. Kanatzidis, J. J. Crochet, J. Even, A. D. Mohite, *Nat. Commun.* **2018**, *9*, 2254.
[13] A. Fieramosca, L. Polimeno, V. Ardizzone, L. De Marco, M. Pugliese, V. Maiorano, M. De Giorgi, L. Dominici, G. Gigli, D. Gerace, D. Ballarini, D. Sanvitto, *Sci. Adv.* **2019**, *5*, 1.
[14] B. Saparov, D. B. Mitzi, *Chem. Rev.* **2016**, *116*, 4558.
[15] D. B. Straus, C. R. Kagan, *J. Phys. Chem. Lett.* **2018**, *9*, 1434.
[16] M. Cinquino, A. Fieramosca, R. Mastria, L. Polimeno, A. Moliterni, V. Olieric, N. Matsugaki, R. Panico, M. D. Giorgi, G. Gigli, C. Giannini, A. Rizzo, D. Sanvitto, L. D. Marco, *Adv. Mater.* **2021**, *33*, 2102326.
[17] K. J. Riisnaes, L. de Marco, L. Polimeno, M. Craciun, S. Russo, *Frontiers in Optics/Laser Science* (Eds.: B. Lee, C. Mazzali, K. Corwin, R. Jason Jones), OSA Technical Digest (Optica Publishing Group, **2020**), paper FTu6B.4.
[18] C. H. Lin, B. Cheng, T. Y. Li, J. R. D. Retamal, T. C. Wei, H. C. Fu, X. Fang, J. H. He, *ACS Nano* **2019**, *13*, 1168.
[19] N. Lamers, Z. Zhang, J. Wallentin, *ACS Appl. Nano Mater.* **2022**, *5*, 3177.
[20] T. L. Leung, I. Ahmad, A. A. Syed, A. M. C. Ng, J. Popović, A. B. Djurišić, *Commun. Mater.* **2022**, *3*, 63.
[21] X. Li, J. M. Hoffman, M. G. Kanatzidis, *Chem. Rev.* **2021**, *121*, 2230.
[22] A. Coriolano, L. Polimeno, M. D. Giorgi, F. Todisco, R. Mastria, V. Ardizzone, L. Dominici, D. Ballarini, A. Rizzo, G. Gigli, D. Sanvitto, L. D. Marco, *Nanomaterials* **2021**, *11*, 1.
[23] I. García-Benito, C. Quarti, V. I. Queloz, Y. J. Hofstetter, D. Becker-Koch, P. Caprioglio, D. Neher, S. Orlandi, M. Cavazzini, G. Pozzi, J. Even, M. K. Nazeeruddin, Y. Vaynzof, G. Grancini, *Front. Chem.* **2020**, *7*, 946.
[24] Y. Wei, P. Audebert, L. Galmiche, J.-S. Lauret, E. Deleporte, *J. Phys. D: Appl. Phys.* **2013**, *46*, 135105.

[25] F. Zhang, D. H. Kim, H. Lu, J.-s. Park, B. W. Larson, J. Hu, L. Gao, C. Xiao, O. G. Reid, X. Chen, Q. Zhao, P. F. Ndione, J. J. Berry, W. You, A. Walsh, M. C. Beard, K. Zhu, *J. Am. Chem. Soc.* **2019**, *141*, 5972.
[26] Y. Tu, Y. Xu, J. Li, Q. Hao, X. Liu, D. Qi, C. Bao, T. He, F. Gao, W. Zhang, *Small* **2020**, *16*, 1.
[27] C. Bao, Z. Chen, Y. Fang, H. Wei, Y. Deng, X. Xiao, L. Li, J. Huang, *Adv. Mater.* **2017**, *29*, 1703209.
[28] A. Fieramosca, L. De Marco, M. Passoni, L. Polimeno, A. Rizzo, B. L. T. Rosa, G. Cruciani, L. Dominici, M. De Giorgi, G. Gigli, L. C. Andreani, D. Gerace, D. Ballarini, D. Sanvitto, *ACS Photonics* **2018**, *5*, 4179.
[29] L. Polimeno, G. Lerario, M. D. Giorgi, L. D. Marco, L. Dominici, F. Todisco, A. Coriolano, V. Ardizzone, M. Pugliese, C. T. Prontera, V. Maiorano, A. Moliterni, C. Giannini, V. Olieric, G. Gigli, D. Ballarini, Q. Xiong, A. Fieramosca, D. D. Solnyshkov, G. Malpuech, D. Sanvitto, *Nat. Nanotechnol.* **2021**, *16*, 1349.
[30] K. Kikuchi, Y. Takeoka, M. Rikukawa, K. Sanui, *Curr. Appl. Phys.* **2004**, *4*, 599.
[31] N. Mercier, N. Louvain, W. Bi, *CrystEngComm* **2009**, *11*, 720.
[32] G. Kresse, J. Furthmüller, *Phys. Rev. B* **1996**, *54*, 11169.
[33] A. V. Krukau, O. A. Vydrov, A. F. Izmaylov, G. E. Scuseria, *J. Chem. Phys.* **2006**, *125*, 224106.
[34] a) A. De Sanctis, J. D. Mehew, S. Alkhalifa, F. Withers, M. F. Craciun, S. Russo, *Nano Lett.* **2018**, *18*, 7919; b) E. G. Moloney, V. Yeddu, M. I. Saidaminov, *ACS Mater. Lett.* **2020**, *2*, 1495.
[35] S. Kahmann, E. K. Tekelenburg, H. Duim, M. E. Kamminga, M. A. Loi, *Nat. Commun.* **2020**, *11*, 2344.
[36] a) N. Peimyoo, H. Y. Wu, J. Escolar, A. De Sanctis, G. Prando, F. Vollmer, F. Withers, A. C. Riis-Jensen, M. F. Craciun, K. S. Thygesen, S. Russo, *ACS Appl. Mater. Interfaces* **2020**, *12*, 55134; b) A. C. Riis-Jensen, M. N. Gjerding, S. Russo, K. S. Thygesen, *Phys. Rev. B* **2020**, *102*, 201402.
[37] *Collective Excitations in Solids* (Ed.: B. Baldassarre), Springer US, New York **1983**.
[38] A. Simbula, L. Wu, F. Pitzalis, R. Pau, S. Lai, F. Liu, S. Matta, D. Marongiu, F. Quochi, M. Saba, A. Mura, G. Bongiovanni, *Nat. Commun.* **2023**, *14*, 4125.
[39] Z. Xu, Y. Yu, S. Arya, I. A. Niaz, Y. Chen, Y. Lei, M. A. R. Miah, J. Zhou, A. C. Zhang, L. Yan, S. Xu, K. Nomura, Y.-H. Lo, *Nano Lett.* **2020**, *20*, 2144.
[40] G. Delport, G. Chehade, F. Lédée, H. Diab, C. Milesi-Brault, G. Trippé-Allard, J. Even, J.-S. Lauret, E. Deleporte, D. Garrot, *J. Phys. Chem. Lett.* **2019**, *10*, 5153.
[41] C. Li, J. Li, Z. Li, H. Zhang, Y. Dang, F. Kong, *Nanomaterials* **2021**, *11*, 1038.
[42] a) A. De Sanctis, J. D. Mehew, M. F. Craciun, S. Russo, *Materials* **2018**, *11*, 1762; b) G. F. Jones, R. M. Pinto, A. De Sanctis, V. K. Nagareddy, C. D. Wright, H. Alves, M. F. Craciun, S. Russo, *Adv. Mater.* **2017**, *29*, 1702993.
[43] J. Jiang, C. Ling, T. Xu, W. Wang, X. Niu, A. Zafar, Z. Yan, X. Wang, Y. You, L. Sun, J. Lu, J. Wang, Z. Ni, *Adv. Mater.* **2018**, *30*, 1804332.
[44] S. F. S. S. F. Soares, *Jpn. J. Appl. Phys.* **1992**, *31*, 210.
[45] L. M. Biberman, *Natural Levels of Illumination and Irradiance*, Springer US, New York **1971**, pp. 39–67.
[46] a) P. Hartnagel, T. Kirchartz, *Adv. Theory Simul.* **2020**, *3*, 2000116; b) S. Zeiske, W. Li, P. Meredith, A. Armin, O. J. Sandberg, *Cell Rep. Phys. Sci.* **2022**, *3*, 101096.
[47] M. Kober-Czerny, S. G. Motti, P. Holzhey, B. Wenger, J. Lim, L. M. Herz, H. J. Snaith, *Adv. Funct. Mater.* **2022**, *32*, 2203064.
[48] J. Gao, Q. Liang, G. Li, T. Ji, Y. Liu, M. Fan, Y. Hao, S. F. Liu, Y. Wu, Y. Cui, *J. Mater. Chem. C* **2019**, *7*, 8357.
[49] Y. Liu, Y. Zhang, Z. Yang, H. Ye, J. Feng, Z. Xu, X. Zhang, R. Munir, J. Liu, P. Zuo, Q. Li, M. Hu, L. Meng, K. Wang, D. M. Smilgies, G. Zhao, H. Xu, Z. Yang, A. Amassian, J. Li, K. Zhao, S. F. Liu, *Nat. Commun.* **2018**, *9*, 5309.
[50] Y. Zhang, Y. Liu, Z. Xu, Z. Yang, S. Liu, *Small* **2020**, *16*, 2003145.
[51] Y. Liu, H. Ye, Y. Zhang, K. Zhao, Z. Yang, Y. Yuan, H. Wu, G. Zhao, Z. Yang, J. Tang, Z. Xu, S. F. Liu, *Matter* **2019**, *1*, 465.
[52] Z. Xu, Y. Li, X. Liu, C. Ji, H. Chen, L. Li, S. Han, M. Hong, J. Luo, Z. Sun, *Adv. Opt. Mater.* **2019**, *7*, 1900308.
[53] Y. Zhao, Y. Qiu, H. Gao, J. Feng, G. Chen, L. Jiang, Y. Wu, *Adv. Mater.* **2020**, *32*, 1905298.
[54] C. Li, H. Wang, F. Wang, T. Li, M. Xu, H. Wang, Z. Wang, X. Zhan, W. Hu, L. Shen, *Light: Sci. Appl.* **2020**, *9*, 31.
[55] G. Tong, X. Geng, Y. Yu, L. Yu, J. Xu, Y. Jiang, Y. Sheng, Y. Shi, K. Chen, *RSC Adv.* **2017**, *7*, 18224.
[56] X. Feng, M. Tan, M. Li, H. Wei, B. Yang, *Nano Lett.* **2021**, *21*, 1500.
[57] C. Bao, J. Yang, S. Bai, W. Xu, Z. Yan, Q. Xu, J. Liu, W. Zhang, F. Gao, *Adv. Mater.* **2018**, *30*, 1803422.
[58] L. Shen, Y. Fang, D. Wang, Y. Bai, Y. Deng, M. Wang, Y. Lu, J. Huang, *Adv. Mater.* **2016**, *28*, 10794.
[59] H. Jing, R. Peng, R. M. Ma, J. He, Y. Zhou, Z. Yang, C. Y. Li, Y. Liu, X. Guo, Y. Zhu, D. Wang, J. Su, C. Sun, W. Bao, M. Wang, *Nano Lett.* **2020**, *20*, 7144.
[60] L. Lin, Y. Liu, W. Wu, L. Huang, X. Zhu, Y. Xie, H. Liu, B. Zheng, J. Liang, X. Sun, C. Zhu, G. Wu, Q. Shuai, Z. Huang, T. Wang, D. Li, A. Pan, *Adv. Electron. Mater.* **2023**, *9*, 2300106.
[61] Y. Fu, M. Yuan, Y. Zhao, M. Dong, Y. Guo, K. Wang, C. Jin, J. Feng, Y. Wu, L. Jiang, *Adv. Funct. Mater.* **2023**, *33*, 2214094.
[62] Alphalas ultrafast photodetectors, https://www.alphalas.com/images/stories/products/laser_diagnostic_tools/Ultrafast_Photodetectors_UPD_ALPHALAS.pdf (accessed: April 2023).
[63] S. Waltersperger, V. Olieric, C. Pradervand, W. Glettig, M. Salathe, M. R. Fuchs, A. Curtin, X. Wang, S. Ebner, E. Panepucci, T. Weinert, C. Schulze-Briese, M. Wang, *J. Synchrotron Radiat.* **2015**, *22*, 895.
[64] W. Kabsch, *Acta Crystallogr., Sect. D* **2010**, *66*, 125.
[65] A. De Sanctis, G. F. Jones, N. J. Townsend, M. F. Craciun, S. Russo, *Rev. Sci. Instrum.* **2017**, *88*, 055102.
[66] J. P. Perdew, K. Burke, M. Ernzerhof, *Phys. Rev. Lett.* **1996**, *77*, 3865.
[67] C.-T. Tsai, *J. Appl. Phys.* **2018**, *123*, 183103.
[68] M. Fox, *Optical Properties of Solids*, second edi edition, Oxford University Press, Oxford **2010**, pp. 95–110.
[69] T. Dammak, M. Koubaa, K. Boukheddaden, H. Bougzhala, A. Mlayah, Y. Abid, *J. Phys. Chem. C* **2009**, *113*, 19305.